photonics

MDPI

Communication

Broadening the Bandwidth of Epsilon-Near-Zero Metamaterials with Embedded Square Frames

Anatoliy V. Goncharenko [1,2,*] and Vyacheslav M. Silkin [2,3,4]

[1] V.E. Lashkaryov Institute of Semiconductor Physics, Nauky Ave. 41, 03028 Kyiv, Ukraine
[2] Donostia International Physics Center (DIPC), Paseo de Manuel Lardizabal 4, 20018 San Sebastian, Spain; vyacheslav.silkin@ehu.es
[3] Departamento de Polímeros y Materiales Avanzados: Física, Química y Tecnología, Facultad de Ciencias Químicas, Universidad del País Vasco UPV/EHU, 20080 San Sebastian, Spain
[4] IKERBASQUE, Basque Foundation for Science, 48013 Bilbao, Spain
* Correspondence: avg@isp.kiev.ua

Abstract: A narrow frequency bandwidth of epsilon-near-zero metamaterials limits the use of many optical, microwave, and electronic devices. In this paper, we propose a recipe to broaden the operational bandwidth by employing a structure of properly tailored square frames nested within each other. To illustrate this effect, we derive the effective permittivity for the considered frame geometry. Then, we show that combining constituent materials with loss and materials with gain enables us to achieve the effective permittivity over a frequency band as small as desired. This technique may prove valuable for various applications including invisibility cloaks, camouflage, shielding, and sensorics.

Keywords: epsilon-near-zero metamaterials; effective permittivity; effective conductivity; square frames

1. Introduction

Many existing devices face limitations in operational bandwidth, and several promising effects remain restricted by stringent material requirements [1]. Among those devices, broadband metalenses [2], holograms [3], and absorbers [4–6] deserve to be mentioned. The above limitation is particularly true also for epsilon near-zero (ENZ) metamaterials (MMs), a relatively new class of macroscopically homogeneous periodic structures with low and ultralow permittivity that exhibit remarkable optical, electrical, and thermal properties. In particular, tunable photonic MMs and devices can be regarded a current trend in the research and applications of ENZ MMs [7–12].

The first known attempt to address bandwidth limitations was made in [13]. The key idea was that in a multiphase periodic system of parallel layers, where the effective permittivity is the weighted harmonic mean of individual layer permittivities (with the electric field normal to the layers), the nullification of individual permittivities across a frequency band enables the ENZ condition over the entire band. This concept was later adapted for various microgeometries, including quasi-1D configurations [14,15] and multilayered stacks [16]. In these studies, each layer was treated as a composite with permittivity defined by the weighted arithmetic mean of its constituents.

Another approach reported in [17] described a broadband near-zero index and ENZ MM for microwave applications. This design utilized two double-layer arrays of subwavelength scatterers on either side of a dielectric sheet, separated by an air cavity.

In [18,19], the Hashin–Shtrikman geometry was applied, in which the composite material consists of coated spheres (or coated cylinders in 2D) [20]. However, from a practical standpoint, this method is questionable because filling the entire volume would require spheres of varying sizes, including infinitesimally small ones.

check for updates

Citation: Goncharenko, A.V.; Silkin, V.M. Broadening the Bandwidth of Epsilon-Near-Zero Metamaterials with Embedded Square Frames. *Photonics* **2024**, *11*, 1185. https://doi.org/10.3390/photonics11121185

Received: 1 November 2024
Revised: 9 December 2024
Accepted: 16 December 2024
Published: 18 December 2024

In [9], a plasmonic MM composed of a series of nanometrically controlled copper/copper oxide nanorods with ultra-broad and reversible ENZ tunability in the visible range was introduced in [9].

An all-dielectric 3D anisotropic near-zero index MM was proposed in [21]. This design is based on a silicon photonic crystal exhibiting dual semi-Dirac cones in the mid-IR range.

There has also been interest in isotropic 3D nanocomposites with a broadband ENZ response. These include suspensions of binary metal alloy nanospheres [22], core–shell nanospheres [23], and randomly oriented metal nanospheroids [24]. However, in these cases, achieving near-zero effective permittivity often requires operating in the resonant regime, potentially leading to high losses. Thus, while the real part of the effective permittivity can approach zero over a frequency range, the imaginary part remains substantial and cannot be ignored.

Interestingly, isotropic 2D nanostructures have not yet been considered in the context of broadband ENZ MMs. This study addresses that gap by introducing a new class of isotropic multiphase MMs composed of embedded square frames, enabling near-zero permittivity across a frequency band in the quasistatic regime. This structure can be viewed as a natural extension of the 1D configurations previously studied. However, our approach differs conceptually: in the 1D case, effective permittivity or conductivity can theoretically be nullified across the entire band, while in the 2D case it can only be nullified at a single frequency but minimized across the band as desired. This concept lays the groundwork for practical 3D broadband ENZ MMs, which hold significant application potential.

2. Basic Concept, Problem Formulation, Assumptions, and Restrictions

In this work, we consider a periodic multiphase system of shelled squares serving as unit cells (or metaatoms). Being tightly packed, the unit cells form an MM. Each square contains $n-1$ shells (frames) with thicknesses t_i and permittivities $\epsilon_1, \epsilon_2, ..., \epsilon_{n-1}$ or conductivities $\sigma_1, \sigma_2, ..., \sigma_{n-1}$, respectively. The innermost square has a permittivity ϵ_n or conductivity σ_n. Thus, the first phase can be treated as a host, while all other phases as inclusions.

For simplicity, we assume a unit cell size of 1×1. The volume fractions of the frames are $f_1 = 4t_1(1-t_1)$, $f_2 = 4t_2(1-2t_1-t_2), ..., f_i = 4t_i(1-2t_1-2t_2-...-t_i)$, and the innermost square volume fraction is $f_n = 1 - \sum_{i=1}^{n-1} f_i$.

Illustrative examples of the unit cells for $n = 2$ and $n = 3$ are shown in Figure 1a,c, respectively. The direction of the electric field is indicated by an arrow.

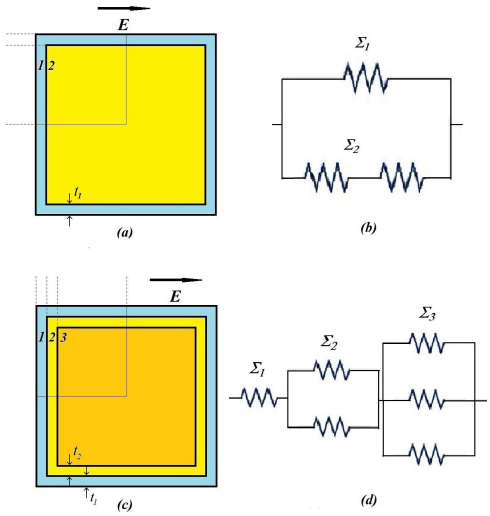

Figure 1. The unit cell of the designed MM for $n = 2$ (**a**) and $n = 3$ (**c**). The dashed lines show the horizontal and vertical arrangements of the layers for $n = 2$ and $n = 3$, respectively. (**b**,**d**) represent the corresponding equivalent circuit diagrams.

Our study relies on the following assumptions:

- All phases are assumed to be nonmagnetic.
- Interfacial resistance is neglected.
- We use the quasi-static approximation and ignore potential non-local effects.

These assumptions can generally be relaxed if needed; they do not fundamentally alter the core concept. So, the effects of nonlocality on the enhancement of broadband nonlinearity for 1D MMs have been addressed in [25]. However, in many cases, nonlocal effects cannot be neglected. In particular, at microwave and lower frequencies, artificial magnetism can occur in various composite structures, including inherently non-magnetic square rings and wire media. In turn, it can give rise to strong non-locality, even for very long wavelengths. At the same time, nonlocal effects are rather sensitive to the presence of losses and cannot be detected if the loss is large enough [26].

The concept of ENZ MMs may assume that either the real part or the modulus of permittivity are close to zero. We focus mainly on the latter case, which provides low or near-zero values of the refractive index. Such MMs are of special practical interest, particularly for the broadband enhancement of optical nonlinearity [25], invisibility cloaking [27], and the enhancement of directivity of beamforming devices [28].

To outline our approach, let us first consider Figure 1a. If ϵ_1(or σ_1) is zero at $\omega = \omega_1$, the effective permittivity $\tilde{\epsilon}$ (or conductivity $\tilde{\sigma}$) of the MM also becomes zero, regardless of ϵ_2(or σ_2). This is because the outer shell blocks the displacement or electric current flow through the MM entirely. Now, consider a nearby frequency ω_2 where ϵ_1(or σ_1) $\neq 0$ and ϵ_2(or σ_2) $= 0$. Generally, the effective permittivity or conductivity will be nonzero at this frequency. However, as the thickness $t \to 0$, $\tilde{\epsilon}(\tilde{\sigma}) \to \epsilon_2(\sigma_2)$. Therefore, to achieve $\tilde{\epsilon}$ or $\tilde{\sigma}$ close to zero at two proximate frequencies, it suffices to have $\epsilon_2(\omega_2) \approx 0$ or $\sigma_2(\omega_2) \approx 0$.

As can be readily observed, the approach described above can be extended to recursively nested frames for any $n > 2$. Formally, this enables us to achieve $\tilde{\epsilon}(\omega_1) = 0, \tilde{\epsilon}(\omega_2) \approx 0, \ldots,$ $\tilde{\epsilon}(\omega_n) \approx 0$ for frequencies $\omega_1, \ldots, \omega_n$ within the frequency band $[\omega_1, \omega_n]$. However, in practice, zeros in the permittivity of real materials are typically associated with energy losses, that complicates the problem. An approach to overcoming this difficulty is to incorporate gain materials to compensate for the losses.

3. Effective Parameters of Embedded Frames

Formally, the effective permittivity $\tilde{\epsilon}$, electric and thermal conductivity $\tilde{\sigma}$ can be derived in a similar way. However, an essential feature of effective permittivity is that the spectrum of $\tilde{\epsilon}(\epsilon_2/\epsilon_1)$ $(n = 2)$ contains branch cuts that must lie on the negative real axis of ϵ_2/ϵ_1 [29]. In order to be definite, in this section we consider the problem in terms of the electric conductivity.

The effective conductivity $\tilde{\sigma}$ can be represented simply as the total conductance of the unit cell. At $n = 2$ (see Figure 1a), it can be evaluated using various techniques [30–37]. Of greatest interest to us is the method proposed in [35]. In essence, this method of treatment reduces the problem to one dimension.

Using the symmetry of the problem, it is convenient to consider only one quadrant of the unit cell. Then, each quadrant can be broken down into two layers, either horizontal or vertical. The horizontal layers are shown in Figure 1a by the dashed lines. Having horizontal layers, we have two conductances in parallel (see Figure 1b), and the total conductance is $\Sigma_{\|} = \Sigma_1 + \Sigma_2$. In turn, Σ_1 is simply

$$\Sigma_1 = 2t_1\sigma_1, \tag{1}$$

while Σ_2 is two conductances in series,

$$\Sigma_2 = \left(\frac{2t_1}{1-2t_1}\frac{1}{\sigma_1} + \frac{1}{\sigma_2}\right)^{-1}. \tag{2}$$

As a result, one has

$$\Sigma_{\parallel} = 2t_1\sigma_1 + \frac{\sigma_1\sigma_2}{\sigma_1 + \sigma_2\frac{2t_1}{1-2t_1}}. \quad (3)$$

At $t_1 \ll 1$, f_1 can be evaluated as $f_1 \approx 4t_1$, and then

$$\Sigma_{\parallel} \approx \frac{1}{2}f_1\sigma_1 + \frac{\sigma_1\sigma_2}{\sigma_1 + \frac{1}{2}f_1\sigma_2}. \quad (4)$$

As is easy to check, our Equation (3) is analogous to Equation (4) from Ref. [35], which is written in terms of resistivity.

Dealing with vertical layers, we have two conductances in series (not shown in Figure 1), and the total conductance is $\Sigma_{\perp} = \left(\Sigma_1^{-1} + \Sigma_2^{-1}\right)^{-1}$, where

$$\Sigma_1 = \frac{\sigma_1}{2t_1} \quad (5)$$

and

$$\Sigma_2 = \frac{2t_1\sigma_1}{1-2t_1} + \sigma_2. \quad (6)$$

The total conductance can then be written as

$$\Sigma_{\perp} = \left(\frac{2t_1}{\sigma_1} + \frac{1}{\sigma_1\frac{2t_1}{1-2t_1} + \sigma_2}\right)^{-1}. \quad (7)$$

Our Equation (7) is in agreement with Equation(3) from Ref. [35].

As was shown, at $f_1 \ll 1$, both Equations (3) and (7) are good approximations for the effective conductivity, $\tilde{\sigma} \approx \Sigma_{\parallel} \approx \Sigma_{\perp}$. At the same time, the geometric mean

$$\tilde{\sigma} \approx \sqrt{\Sigma_{\parallel}\Sigma_{\perp}} \quad (8)$$

provides an even better approximation for the effective conductivity, which is rather accurate for any f_1 except for that close to unity [35]. In general, as f_1 is not too small, the approximation $\Sigma_{\parallel} \approx \Sigma_{\perp}$ is no longer valid. Anyway, the relative error of Equation (8) with reference to finite element modeling does not exceed 5% over the entire range of f_1, does not exceed 3% at $f_1 < 80\%$, does not exceed 1% at $f_1 < 2\%$, and decreases rapidly as $f_1 \to 0$, being almost independent of the σ_2/σ_1 ratio.

Let us now consider the case of $n = 3$, i.e., two embedded frames (see Figure 1 c). For the horizontal arrangement of layers, the total conductance includes three conductances in parallel, as shown in Figure 1d for the left upper quadrant. Then, $\Sigma_{\parallel} = \Sigma_1 + \Sigma_2 + \Sigma_3$, where Σ_1 is the same as in Equation (1), while

$$\Sigma_2 = \left(\frac{t_1}{t_2}\frac{1}{\sigma_1} + \frac{1-2t_1}{2t_2}\frac{1}{\sigma_2}\right)^{-1} = t_2\left(\frac{t_1}{\sigma_1} + \frac{1-2t_1}{2}\frac{1}{\sigma_2}\right)^{-1}, \quad (9)$$

and

$$\Sigma_3 = \left(\frac{t_1}{1-2t_1-2t_2}\frac{2}{\sigma_1} + \frac{t_2}{1-2t_1-2t_2}\frac{2}{\sigma_2} + \frac{1}{\sigma_3}\right)^{-1}. \quad (10)$$

At $t_1 \ll 1$ and $t_2 \ll 1$, this yields the following result:

$$\Sigma_{\parallel} \approx \frac{1}{2}f_1\sigma_1 + \frac{f_2\sigma_1\sigma_2}{f_2\sigma_2 + 2\sigma_1} + \frac{(2-f_1-f_2)\sigma_1\sigma_2\sigma_3}{f_1\sigma_2\sigma_3 + f_2\sigma_1\sigma_3 + (2-f_1-f_2)\sigma_1\sigma_2} \approx \frac{1}{2}(f_1\sigma_1 + f_2\sigma_2) + \sigma_3. \quad (11)$$

In the general case, as the unit cell contains n phases and correspondingly includes $n-1$ frames,

$$\Sigma_{\parallel} = \sum_{i=1}^{n} \Sigma_i. \tag{12}$$

The partial conductances Σ_i can easily be calculated. So, Σ_1 is always the same as in Equation (1), while

$$\Sigma_i = \left[\frac{t_1}{t_i} \frac{1}{\sigma_1} + ... \frac{t_{i-1}}{t_i} \frac{1}{\sigma_{i-1}} + \frac{1 - 2t_1 - ... - 2t_{i-1}}{2t_i} \frac{1}{\sigma_i} \right]^{-1} \tag{13}$$

for $1 < i < n$ and

$$\Sigma_n = \left[\frac{2t_1}{1 - 2t_1 - ... - 2t_{n-1}} \frac{1}{\sigma_1} + ... \frac{2t_{n-1}}{1 - 2t_1 - ... - 2t_{n-1}} \frac{1}{\sigma_{n-1}} + \frac{1}{\sigma_n} \right]^{-1}. \tag{14}$$

In a similar manner, for the vertical arrangement, at $n = 3$, Σ_1 is the same as in Equation (5), while

$$\Sigma_2 = \frac{t_1}{t_2}\sigma_1 + \frac{1 - 2t_1}{2t_2}\sigma_2 = \frac{1}{t_2}\left(t_1\sigma_1 + \frac{1 - 2t_1}{2}\sigma_2 \right), \tag{15}$$

and

$$\Sigma_3 = \frac{2t_1\sigma_1}{1 - 2t_1 - 2t_2} + \frac{2t_2\sigma_2}{1 - 2t_1 - 2t_2} + \sigma_3. \tag{16}$$

At $t_1 \ll 1$ and $t_2 \ll 1$, this yields

$$\Sigma_{\perp} \approx \left(\frac{f_1}{2\sigma_1} + \frac{f_2}{2\sigma_2} + \frac{1}{\sigma_3} \right)^{-1}. \tag{17}$$

In the general case,

$$\Sigma_{\perp} = \left(\sum_{i=1}^{n} \Sigma_i^{-1} \right)^{-1} \tag{18}$$

with Σ_1 as in Equation (5), while

$$\Sigma_i = \frac{t_1}{t_i}\sigma_1 + ... + \frac{t_{i-1}}{t_i}\sigma_{i-1} + \frac{1 - 2t_1 - ... - 2t_{i-1}}{2t_i}\sigma_i \tag{19}$$

for $1 < i < n$ and

$$\Sigma_n = \frac{2t_1\sigma_1}{1 - 2t_1 - ... - 2t_{n-1}} + ... + \frac{2t_{n-1}\sigma_{n-1}}{1 - 2t_1 - ... - 2t_{n-1}} + \sigma_n. \tag{20}$$

As one can check, the effective conductivity determined in accordance with Equation (8), where $\Sigma_{\parallel}$ and $\Sigma_{\perp}$ are specified by Equations (12) and (18), respectively, satisfies the duality relation (generalized Keller's theorem) [38]

$$\tilde{\sigma}(\sigma_i^{-1}) = 1/\tilde{\sigma}(\sigma_i). \tag{21}$$

In fact, after the interchange of $\sigma_i \to 1/\sigma_i$, one has $\sigma_{\parallel} \to 1/\sigma_{\perp}$ and $\sigma_{\perp} \to 1/\sigma_{\parallel}$, which yields $\tilde{\sigma} \to 1/\tilde{\sigma}$.

As far as the 1D approximation, Equation (8), works well, especially at $t \ll 1$, we show that it can provide the needed condition of nulling $\tilde{\sigma}$ through a frequency band. With this aim, consider first the term $\Sigma_{\parallel}$.

In Equation (12), the term Σ_1 is always small because it is zero (if $\sigma_1 = 0$) or $\Sigma_1 \propto t \ll 1$. In Equation (13), $\Sigma_i \ll 1$ only if any of the conductivities $\sigma_1, ..., \sigma_i$ is equal to zero. Finally, in Equation (14), the term Σ_n is always small, because it is zero (if $\sigma_n = 0$) or $\Sigma_n \propto t \ll 1$.

Consider then the term $\Sigma_\perp$. In Equation (18), the term Σ_1 is, as before, small. In Equation (19), as $t_i \ll 1$, the term Σ_i is always large, except for the case where $\sigma_i = 0$. Finally, in Equation (20), the term Σ_n is always small. This provides the condition $\Sigma_\perp \ll 1$ if either $\sigma_1 = 0$ or $\sigma_n = 0$.

Ultimately, either $\Sigma_\parallel$ or $\Sigma_\perp$ is small through the band $[\omega_1, ..., \omega_n]$, where $\sigma_i(\omega_i) = 0$. This, in accordance with Equation (8), provides the needed condition $\tilde{\sigma} \ll 1$ within the band.

4. Numerical Analysis and Discussion

At this point, it is valuable to complement the preceding analysis with numerical simulations. When working with ENZ MMs, it is essential to account for the impact of losses, as these can significantly influence the nulling of the effective permittivity and often cannot be disregarded. This gives rise to the complex-valued permittivity, which adds complexity to our consideration. Nonetheless, with an appropriate design and careful selection of materials, it becomes possible to achieve effective broadband reduction in $\tilde{\epsilon}$.

One of the approaches involves combining plasmonic and dielectric materials, where $\Re\epsilon_i < 0$ and $\Re\epsilon_i > 0$, respectively. In addition, losses can be controlled through various compensation mechanisms, such as incorporating gain molecules or quantum dots (see, e.g., [39–42]).

As an example, we consider a periodic MM with a unit cell in the form of embedded frames, where high doping with aluminum zinc oxide (AZO) is taken as a host phase. The permittivity of AZO in the near IR is of the Drude type

$$\epsilon_1 = \epsilon_\infty - \frac{\omega_p^2}{\omega^2 + i\omega\gamma}, \tag{22}$$

where $\epsilon_\infty = 3.85$, $\omega_p = 1.747$ eV, and $\gamma = 0.1$ eV, that approximately corresponds to a dopant concentration of 2 wt% [43,44].

As shown in Figure 2, the real part of the permittivity of AZO $\Re\epsilon_1 = 0$ at $\omega_0 \simeq 0.885$ eV and is negative below this point. Notably, the imaginary part of its permittivity, $\Im\epsilon_1$, remains moderately low compared to most other highly doped semiconductors. To be specific, we set the frequency range of interest from 0.75 to 0.8 eV. This provides a bandwidth of about 6.5%.

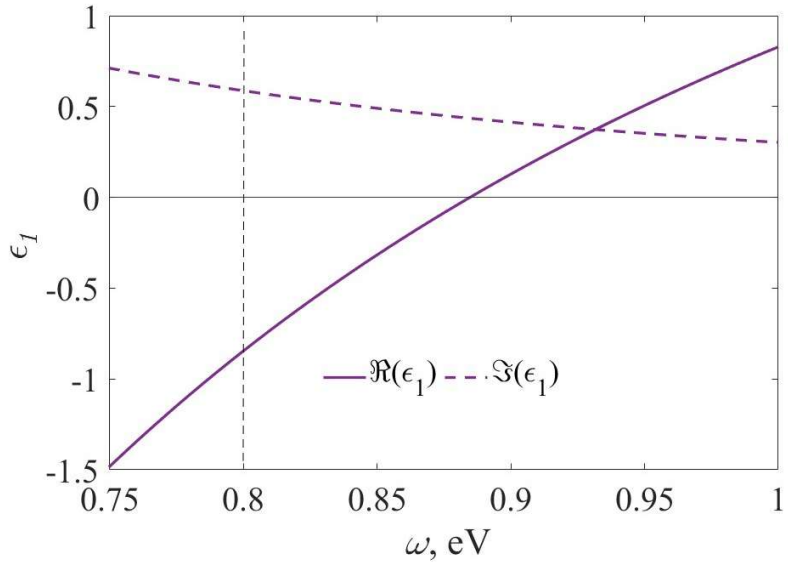

Figure 2. The permittivity of the host phase of the designed MM.

As $\Re\epsilon_1$ is negative within the targeted frequency band and exhibits normal dispersion ($\partial\Re\epsilon_1/\partial\omega > 0$), it is reasonable to assume that at least one of the inclusion phases must have $\Re\epsilon_i > 0$ and exhibit anomalous dispersion ($\partial\Re\epsilon_i/\partial\omega < 0$) within the same band.

Furthermore, since $\Im\epsilon_1 > 0$, compensating for losses can be achieved if at least one of the inclusion phases satisfies the condition $\Im\epsilon_i < 0$. To address this, we consider the permittivity of the inclusions to follow a general Lorentzian form

$$\epsilon_i = \epsilon_0 - \frac{A_i}{\omega - \omega_i + i\Delta_i}, \tag{23}$$

where ϵ_0 is the background permittivity, and A_i, ω_i, and Δ_i represent the transition strength, frequency, and linewidth, respectively. At $A_i > 0$, Equation (23) describes lossy media, while at $A_i < 0$, it describes gain media. For simplicity, we treat all inclusions as gain media and use fixed model parameters in Equation (23), specifically $\epsilon_0 = 1.3$, $A_i = -0.2$, and $\Delta_i = 0.05$ eV. Alongside this, all t_i and ω_i are treated as fitting parameters optimized to minimize the objective function $|\tilde{\epsilon}|$ within the targeted frequency band.

To proceed, let us first consider the simplest case of $n = 2$. The modulus of the effective permittivity of the designed MM, calculated using the model parameters obtained through the fitting procedure, is shown in Figure 3. With the optimal parameter values, $t_1 = 0.127$ and $\omega_2 = 0.983$ eV, the modulus of the effective permittivity $|\tilde{\epsilon}|$ reaches its minimum value of approximately 0.005 at $\omega \approx 0.775$ eV. At the low-frequency and high-frequency edges of the band, $|\tilde{\epsilon}|$ has values of approximately 0.105 and 0.125, respectively. For comparison, the dependencies of $\epsilon_{\parallel}(\omega)$ and $\epsilon_{\perp}(\omega)$ are also shown. In the example presented, the small value of $|\tilde{\epsilon}|$ within the targeted frequency band is achieved mainly due to the small magnitude of the factor $\epsilon_{\perp}$ entering Equation (8), where it is designated as $\Sigma_{\perp}$. The permittivity of the inclusion phase, $\epsilon_2(\omega)$, has a negative slope in the desired frequency band, thereby demonstrating an anomalous dispersion, as expected.

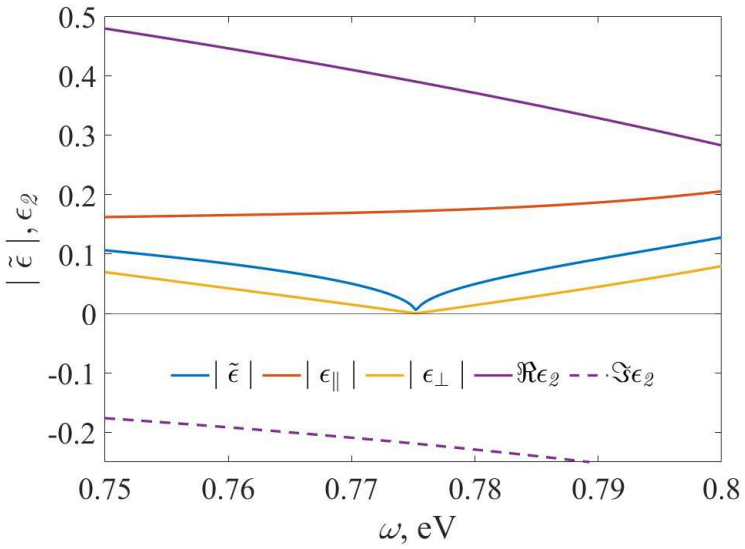

Figure 3. The modulus of the effective permittivity and the permittivity of the inclusion phase of the modeled MM with $n = 2$.

The modulus of the effective permittivity of the designed MM with $n = 3$ and $n = 4$ calculated using model parameters obtained through the fitting procedure is shown in Figure 4. For the three-phase MM ($n = 3$), the optimal parameters are $t_1 = 0.1705$, $t_2 = 0.0114$, $\omega_2 = 0.756$ eV, and $\omega_3 = 0.997$ eV. For four-phase MM ($n = 4$), they are $t_1 = 0.163$, $t_2 = 0.00045$, $t_3 = 0.00947$, $\omega_2 = 0.699$ eV, $\omega_3 = 0.754$ eV, and $\omega_4 = 0.995$ eV.

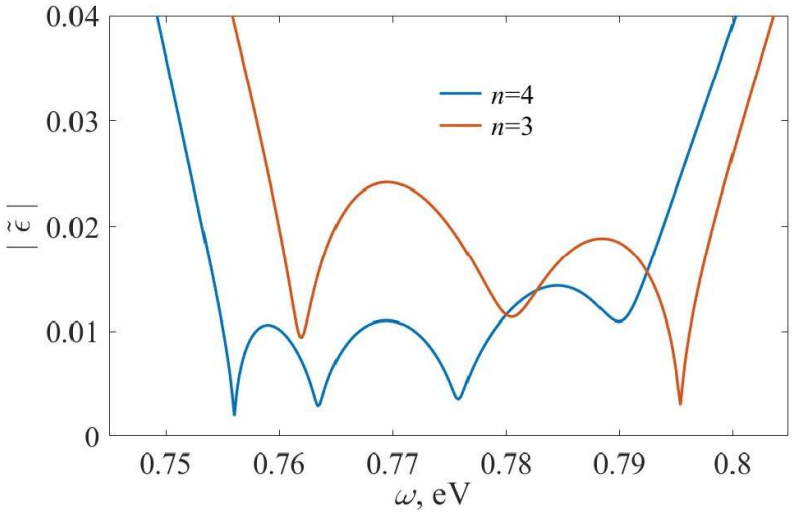

Figure 4. The modulus of the effective permittivity of the modeled MM with $n = 3$ and $n = 4$.

At $n = 3$, the function $\mid \tilde{\epsilon} \mid$ exhibits three local minima within the band. Notably, two of these minima arise from the local minima of $\mid \epsilon_{\parallel} \mid$, while the third is due to $\mid \epsilon_{\perp} \mid$. At $n = 4$, the function $\mid \tilde{\epsilon} \mid$ displays four local minima within the band. Three of these are associated with the minima in $\mid \epsilon_{\parallel} \mid$, while the remaining one corresponds to the minimum in $\mid \epsilon_{\perp} \mid$. As the number of phases—and consequently, the number of degrees of freedom—increases, it becomes possible to achieve $\mid \tilde{\epsilon} \mid$ closer to zero within the targeted band. In general, by increasing the number of inclusion phases, it becomes possible to achieve the effective permittivity over a frequency band as small as desired.

In more general cases, optimization and fitting techniques could be employed to fine-tune the broadband dielectric and optical properties. Depending on the application, it can be prioritized to minimize $\mid \tilde{\epsilon} \mid$, $\mathrm{Re}(\tilde{\epsilon})$, or $\tilde{n} = \mathrm{Re}(\sqrt{\tilde{\epsilon}})$ across a specific frequency band.

Here, we focus on ENZ MMs. Meanwhile, the above results could be useful in a broader context, particularly to develop broadband invisibility cloaks, camouflage and shielding [45–52], as well as for sensor applications [9]. They could be useful for the design of frequency selective surfaces —-periodic structures capable of functioning as low-pass, high-pass, band-pass, and band stop filters when interacting with electromagnetic waves [53]. In the microwave range, as an artificial effective permeability occurs, it is constructive to consider a near-zero refractive index rather than an ENZ MM. On the one hand, this complicates the analysis and design of these MMs, but on the other hand, this opens up new possibilities. So, broadened bandwidth can result not only from small values (zeros) of the effective permittivity but also from small values (zeros) of the effective permeability, which occur slightly above its resonant frequencies.

Although we have dealt with 2D microgeometry, dealing with multishelled cubes would allow us to generalize our approach to the 3D case.

5. Conclusions

We derived closed-form expressions for the effective conductivity and permittivity of two-dimensional metamaterials with recursively nested frames. After that, we numerically demonstrated that incorporating materials with gain to counterbalance losses could significantly reduce the effective permittivity within a specified frequency band. In general, by appropriately selecting the material and geometric parameters, it is possible to achieve arbitrarily low values of effective permittivity across the band.

Future studies could build on this work by extending the approach to three-dimensional configurations. Once the effective permittivity or conductivity for a given microgeometry is established, this framework can facilitate the design of novel metamaterials with customizable broadband optical or electrical properties. We anticipate that similar metamaterials, incorpo-

rating multishelled building blocks, hold significant promise for applications in broadband cloaking, camouflage, electromagnetic shielding, as well as advanced sensor technologies.

Author Contributions: Conceptualization, A.V.G. and V.M.S.; methodology, A.V.G.; software, A.V.G.; validation, A.V.G. and V.M.S.; investigation, A.V.G. and V.M.S.; resources, V.M.S.; writing—original draft preparation, A.V.G.; writing—review and editing, A.V.G. and V.M.S.; supervision, V.M.S.; project administration, V.M.S.; funding acquisition, V.M.S. All authors have read and agreed to the published version of the manuscript.

Funding: This research was partially supported by the Spanish Ministry of Science and Innovation, Grants No. TED2021-132074B-C32 and PID2022-139230NB-I00.

Institutional Review Board Statement: Not applicable.

Informed Consent Statement: Not applicable.

Data Availability Statement: The data presented in this study are available on request from the corresponding author.

Conflicts of Interest: The authors declare no conflicts of interest.

Abbreviations

The following abbreviations are used in this manuscript:

1D	One-dimensional;
2D	Two-dimensional;
3D	Three-dimensional;
AZO	Aluminum zinc oxide;
ENZ	Epsilon-near-zero;
IR	Infrared;
MM	Metamaterial.

References

1. Jung, J.; Park, H.; Park, J.; Chang, T.; Shin, J. Broadband metamaterials and metasurfaces: A review from the perspectives of materials and devices. *Nanophotonics* **2020**, *9*, 3165–3196. [CrossRef]
2. Li, K.; Guo, Y.; Pu, M.; Li, X.; Ma, X.; Zhao, Z.; Luo, X. Dispersion controlling meta-lens at visible frequency. *Opt. Exp.* **2017**, *25*, 21419. [CrossRef] [PubMed]
3. Wang, B.; Dong, F.; Li, Q.T.; Yang, D.; Sun, C.; Chen, J.; Song, Z.; Xu, L.; Chu, W.; Xiao, Y.F.; et al. Visible-frequency dielectric metasurfaces for multiwavelength achromatic and highly dispersive holograms. *Nano Lett.* **2016**, *16*, 5235–5240. [CrossRef] [PubMed]
4. Anopchenko, A.; Tao, L.; Arndt, C.; Lee, H.W.H. Field-effect tunable and broadband epsilon-near-zero perfect absorbers with deep subwavelength thickness. *ACS Photon.* **2018**, *5*, 2631–2637. [CrossRef]
5. Cheng, S.; Li, W.; Zhang, H.; Akhtar, M.N.; Yi, Z.; Zeng, Q.; Ma, C.; Sun, T.; Wu, P.; Ahmad, S. High sensitivity five band tunable metamaterial absorption device based on block like Dirac semimetals. *Opt. Commun.* **2024**, *569*, 130816. [CrossRef]
6. Chen, Z.; Cheng, S.; Zhang, H.; Yi, Z.; Tang, B.; Chen, J.; Zhang, J.; Tang, C. Ultra wideband absorption absorber based on Dirac semimetallic and graphene metamaterials. *Phys. Lett. A* **2024**, *517*, 129675. [CrossRef]
7. Lobet, M.; Kinsey, M.; Liberal, I.; Caglayan, H.; Huidobro, P.A.; Galiffi, E.; Majia-Salazar, J.R.; Palermo, G.; Jacob, Z.; Maccaferri, N. New horizons in near-zero refractive index photonics and hyperbolic metamaterials. *ACS Photon.* **2023**, *10*, 3805–3820. [CrossRef]
8. Lio, G.E.; Ferraro, A.; Zappone, B.; Parka, J.; Schab-Balcerzak, E.; Umeton, C.P.; Riboli, F.; Kowerdziej, R.; Caputo, R. Unlocking optical coupling tunability in epsilon-near-zero metamaterials through jiquid crystal nanocavities. *Adv. Opt. Mater.* **2024**, *12*, 2302483. [CrossRef]
9. Zaleska, A.; Krasavin, A.V.; Zayats, A.V.; Dickson, W. Copper-based core–shell metamaterials with ultra-broadband and reversible ENZ tunability. *Mater. Adv.* **2024**, *5*, 5845–5854. [CrossRef]
10. Zheng, H.; Zheng, Y.; Ouyang, M.; Fan, H.; Dai, Q.; Liu, H.; Wu, L. Electromagnetically induced transparency enabled by quasi-bound states in the continuum modulated by epsilon-near-zero materials. *Opt. Exp.* **2024**, *32*, 7318–7331. [CrossRef]
11. Sun, F.; Shan, J.; Liu, Y.; Zhao, X. Tunable uniform field enhancement in a subwavelength air pillar by photonic doping in epsilon-near-zero medium. *Res. Phys.* **2024**, *61*, 107778. [CrossRef]
12. Mao, Y.; Zhang, H.; Xiong, J.; Liu, X.; Wang, Q.; Wang, J. Controlling of spontaneous emission of quantum dots based on hyperbolic metamaterials. *J. Phys. D Appl. Phys.* **2024**, *57*, 255111. [CrossRef]
13. Goncharenko, A.V.; Chen, K.R. Strategy for designing epsilon-near-zero nanostructured metamaterials over a frequency range. *J. Nanophoton.* **2010**, *4*, 041530. [CrossRef]

14. Goncharenko, A.V.; Nazarov, V.U.; Chen, K.R. Development of metamaterials with desired broadband optical properties. *Appl. Phys. Lett.* **2012**, *101*, 071901. [CrossRef]
15. Sun, L.; Gao, J.; Yang, X. Broadband epsilon-near-zero metamaterials with steplike metal-dielectric multilayer structures. *Phys. Rev. B* **2013**, *87*, 165134. [CrossRef]
16. Sun, L.; Yu, K.W. Strategy for designing broadband epsilon-near-zero metamaterial with loss compensation by gain media. *Appl. Phys. Lett.* **2012**, *100*, 261903. [CrossRef]
17. Konstantinidis, K.; Feresidis, A.P. Broadband near-zero index metamaterials. *J. Opt.* **2015**, *17*, 105104. [CrossRef]
18. Sun, L.; Yu, K.W.; Wang, G.P. Inverse design of broadband epsilon-near-zero metasurface with nanoscale airtube superlattice based on the Bergman-Milton spectral representation. *Phys. Rev. B* **2019**, *100*, 125429. [CrossRef]
19. Sun, L.; Wang, G.P. Broadband epsilon-near-zero metamaterials and its application in optical field manipulation. *Acta Photon. Sin.* **2022**, *51*, 0151107.
20. Hashin, Z.; Shtrikman, S. A variational approach to the theory of the effective magnetic permeability of multiphase materials. *J. Appl. Phys.* **1962**, *31*, 3125–3131. [CrossRef]
21. Sun, B.; Mei, R.; Li, M.; Xu, Y.; Luo, J.; Liu, Y. All-dielectric dual-band anisotropic zero-index materials. *Photonics* **2024**, *11*, 1018. [CrossRef]
22. Goncharenko, A.V.; Nazarov, V.U.; Chen, K.R. Nanostructured metamaterials with broadband optical properties. *Opt. Mater. Exp.* **2013**, *3*, 143–146. [CrossRef]
23. Goncharenko, A.V.; Venger, E.F.; Chang, Y.C.; Pinchuk, A.O. Arrays of core-shell nanospheres as 3D isotropic broadband ENZ and highly absorbing metamaterials. *Opt. Mat. Exp.* **2014**, *4*, 2310–2322. [CrossRef]
24. Goncharenko, A.V.; Pinchuk, A.O. Broadband epsilon-near-zero composites made of metal nanospheroids. *Opt. Mat. Exp.* **2014**, *4*, 1276–1286. [CrossRef]
25. Goncharenko, A.V.; Silkin, V.M.; Chang, Y.C. Nonlinearity vs nonlocality with emphasis on bandwidth broadening in semiconductor-based 1d metamaterials. *Opt. Exp.* **2024**, *32*, 12551–12568. [CrossRef]
26. Wurtz, G.A.; Dickson, W.; Zayats, A.V.; Murphy, A.; Pollard, R.J. Plasmonic nanorod metamaterials as a platform for active nanophotonics. In *Active Plasmonics and Tuneable Plasmonic Metamaterials*; Zayats, A.V., Maier, S.A., Eds.; Wiley: New York, NY, USA, 2013; pp. 69–104.
27. Yao, P.; Liang, Z.; Jiang, X. Limitation of the electromagnetic cloak with dispersive material. *Appl. Phys. Lett.* **2008**, *92*, 031111. [CrossRef]
28. Navarro-Cia, M.; Beruete, M.; Campillo, I.; Sorolla, M. Enhanced lens by ϵ and μ near-zero metamaterial boosted by extraordinary optical transmission. *Phys. Rev. B* **2011**, *83*, 115112. [CrossRef]
29. Helsing, J.; McPhedran, R.C.; Milton, G.W. Spectral super-resolution in metamaterial composites. *New J. Phys.* **2011**, *13*, 115005. [CrossRef]
30. Lu, S.Y. The effective thermal conductivities of composites with 2D arrays of circular and square cylinders. *J. Comp. Mater.* **1995**, *29*, 483–506. [CrossRef]
31. Andrianov, I.V.; Starushenko, G.A.; Danishevs'kyy, V.V.; Tokarzewski, S. Homogenization procedure and Padé approximants for effective heat conductivity of composite materials with cylindrical inclusions having square cross-section. *Proc. R. Soc. Lond. A* **1999**, *455*, 3401–3413. [CrossRef]
32. Wu, F.; Whites, K.W. Quai-static effective permittivity of periodic composites containing complex shaped dielectric particles. *IEEE Trans. Ant. Propag.* **2001**, *49*, 1174–1182.
33. Whites, K.W.; Wu, F. Effects of particle shape on the effective permittivity of composite materials with measurements for lattices of cubes. *IEEE Trans. Microw. Theory Tech.* **2002**, *50*, 1723–1729. [CrossRef]
34. Yariv, E. Conductivity of a medium containing a dense array of perfectly conducting square cylinders. *J. Eng. Math.* **2021**, *127*, 12. [CrossRef]
35. Guralnik, B.; Hansen, O.; Henrichsen, H.H.; Caridad, J.M.; Wilson, W.; Hanse, M.F.; Nielsen, P.F.; Petersen, D.H. Effective electrical resistivity in a square array of oriented square inclusions. *Nanotechnology* **2021**, *32*, 185706. [CrossRef]
36. Goncharenko, A.V.; Venger, E.F. The conductivity of a sheet perforated with square holes. *Phys. Lett. A* **2022**, *434*, 128057. [CrossRef]
37. Ding, Y.Y.; Shuai, Z.; Hua, S.; Xiao-Dong, S. Rayleigh analysis and numerical simulations of metal-mesh/transparent conducting oxide composite transparent electrode. *Acta Phys. Sin.* **2024**, *73*, 146801. [CrossRef]
38. Fel, L.G.; Machavariani, V.S.; Bergman, D.J. Isotropic conductivity of two-dimensional three-component symmetric composites. *J. Phys. A Math. Gen.* **2000**, *33*, 6669–6681. [CrossRef]
39. Webb, K.J.; Ludwig, A. Semiconductor quantum dot mixture as a lossless negative dielectric constant optical material. *Phys. Rev. B* **2008**, *78*, 153303. [CrossRef]
40. Holmström, P.; Thylén, L.; Bratkovsky, A. Composite metal/quantum-dot nanoparticle-array waveguides with compensated loss. *Appl. Phys. Lett. A* **2010**, *97*, 073110.
41. Kirby, E.I.; Hamm, J.M.; Pickering, T.W.; Tsakmakidis, K.L.; Hess, O. Evanescent gain for slow and stopped light in negative refractive index heterostructures. *Phys. Rev. B* **2011**, *84*, 041103. [CrossRef]
42. Veltri, A.; Aradian, A. Optical response of a metallic nanoparticle immersed in a medium with optical gain. *Phys. Rev. B* **2012**, *85*, 115429. [CrossRef]

43. Naik, G.V.; Shalaev, V.M.; Boltasseva, A. Alternative plasmonic materials; beyond gold and silver. *Adv. Mater.* **2013**, *25*, 3264–3294. [CrossRef] [PubMed]
44. Tian, W.; Liang, F.; Chi, S.;Li, C.; Yu, H.; Zhang, H.; Zhang, H. Highly efficient super-continuum generation on an epsilon-near-zero surface. *ACS Omega* **2020**, *5*, 2458–2464. [CrossRef] [PubMed]
45. Sen, H.; Liang, Z.; Yao, P.; Jiang, X.; Ma, H.; Chan, C.T. Extending the bandwidth of electromagnetic cloaks. *Phys. Rev. B* **2007**, *76*, 241104.
46. Alitalo, P.; Tretyakov, S.A. Broadband electromagnetic cloaking realized with transmission-line and waveguiding structures. *Proc. IEEE* **2011**, *99*, 1646–1659. [CrossRef]
47. Klotz, G.; Mallejac, N.; Guenneau, S.; Enoch, S. Controlling frequency dispersion in electromagnetic invisibility cloaks. *Sci. Rep.* **2019**, *9*, 6022. [CrossRef]
48. Chen, A.; Monticone, F. Active scattering-cancellation cloaking: Broadband invisibility and stability constraints. *IEEE Trans. Ant. Propag.* **2020**, *68*, 1655–1664. [CrossRef]
49. Lee, K.T.; Ji, C.; Iizuka, H.; Banerjee, D. Optical cloaking and invisibility: From fiction toward a technological reality. *J. Appl. Phys.* **2021**, *129*, 231101. [CrossRef]
50. Tian, B.; Wang, J.; Dai, G.; Ouyang, X.; Huang, J. Thermal metadevices with geometrically anisotropic heterogeneous composites. *Int. J. Heat Mass Trans.* **2021**, *174*, 121312. [CrossRef]
51. Micheli, D.; Pastore, R.; Vricella, A.; Morles, R.B.; Marchetti, M.; Delfini, A.; Moglie, F.; Mariani Primiani, V. Electromagnetic characterization and shielding effectiveness of concrete composite reinforced with carbon nanotubes in the mobile phones frequency band. *Mater. Sci. Eng. B* **2014**, *188*, 119–129. [CrossRef]
52. Kuruvilla, J.; Runcy, W.; Gejo, G. (Eds.) *Materials for Potential EMI Shielding Applications. Processing, Properties and Current Trends*; Elsevier: Amsterdam, The Netherlands, 2020.
53. Munk, B.A. *Frequency Selective Surfaces-Theory and Design*; Wiley: New York, NY, USA, 2000.